Article

Double-Virtual-Vector-Based Model Predictive Torque Control for Dual Three-Phase PMSM

Qingqing Yuan [1,*], Rongyan Xiao [1], Jingxia Wang [1], Kun Xia [1] and Wei Yu [2]

[1] Department of Electrical Engineering, University of Shanghai for Science and Technology, Shanghai 200093, China; 222221526@st.usst.edu.cn (R.X.); jingxiawang@usst.edu.cn (J.W.); xiakun@usst.edu.cn (K.X.)

[2] Hella Shanghai Electronics Co., Ltd., Shanghai 201201, China; wei.yu.wyu@forvia.com

* Correspondence: yuanqq@usst.edu.cn

Abstract: To overcome the drawbacks of large torque ripples and high harmonic contents in a dual three-phase permanent magnet synchronous motor (PMSM) used in electric vehicle drive systems, a double-virtual-vector-based model predictive torque control (DVV-MPTC) strategy was proposed in this paper. Firstly, 12 virtual voltage vectors were constructed to minimize harmonic interference as much as possible. Then, the DVV-MPTC strategy is proposed to solve the problem of large torque ripples caused by single-virtual-vector-based MPTC (SVV-MPTC) method. On the other hand, an enhancement to the cost function was also introduced to resolve the challenges of tuning weight coefficients. Experimental comparisons between traditional direct torque control (DTC), SVV-MPTC method, and the proposed DVV-MPTC strategy were carried out, which show that the latter achieves significant improvements. In particular, it can reduce both harmonic components and torque ripple compared to traditional control strategies, resulting in a more efficient and stable performance for the electric drive system.

Keywords: dual three-phase motor; double-virtual-vector-based model predictive torque control; harmonic suppression; low torque ripple

1. Introduction

The electric vehicles with advantages such as energy efficiency, emission reduction, high efficiency, and low cost are gradually taking over the market compared to fuel-powered vehicles. In the current electric vehicle industry, traditional three-phase motor drives hold a dominant position. However, they have certain limitations, such as being constrained by bus voltage and the power level of power electronics, making it difficult to meet the demands for high power at a low voltage [1,2]. Therefore, multi-phase motor drives, with advantages like low torque ripple, more flexible control, and fault-tolerant control capability, have begun to attract attention in the electric vehicle field [3–5].

The dual three-phase permanent magnet synchronous motor (DTP-PMSM) is a typical representative of multi-phase motors and is closely related to traditional three-phase motors [6–8]. These DTP-PMSMs have broad application prospects and are increasingly being used in electric vehicles [9–11]. However, it exhibits $6k \pm 1$ ($k = 1, 3, 5, \ldots$) harmonics which cause torque ripples and additional losses.

Direct torque control (DTC) is a high-performance motor control method known for its fast dynamic response, simple control structure, and efficient operation [12,13]. However, it also has drawbacks, such as large torque ripples, variable switching frequency, and dependency on motor parameters. Finite-control-set model predictive control (FCS-MPC)

inherently manages discrete switching states. When applied to PMSMs control, it can be categorized into finite-control-set model predictive torque control (FCS-MPTC) and finite-control-set model predictive current control (FCS-MPCC).

Due to the limitations of basic voltage vectors, the motor's output current and torque may contain significant harmonics. Currently, a large number of studies explored virtual voltage vectors. For instance, in reference [14], a hexagonal coordinate system was introduced to construct virtual voltage vectors to enhance the motor control system's performance and expand the predictive control set. In [15], the authors synthesized virtual voltage vectors using three basic voltage vectors with minimal common-mode voltage to suppress common-mode voltage. In [16], 12 virtual voltage vectors were constructed based on the principle that the magnitude of the virtual voltage vector in the x-y harmonic plane is zero, achieving harmonic suppression. In [17], a total of 72 virtual voltage vectors were synthesized based on the principle that the same basic voltage vectors have opposite directions in different sub-planes. Multiple virtual voltage vectors were applied in DTC to reduce torque ripples.

Currently, there is numerous research on FCS-MPTC for three-phase PMSMs, and it has been extended to DTP-PMSM drive systems as well [18]. In [19], to address the issue of significant flux and torque ripple inherent in DTC, a dual-voltage vector MPTC (DV-MPTC) method was proposed, in which the predictive voltage vector was synthesized using two basic voltage vectors, and the numbers of predictive voltage vectors were reduced from 12 to 4. However, this approach still suffered from relatively large torque ripples and had difficulty in tuning the weight coefficients in the cost function. Ref. [20] proposed a type of two-vector dimensionless MPTC. The paper employed fuzzy decision-making to eliminate the weighting factors from the two torque and flux cost functions and selected two optimal voltage vectors. The torque error determined the duty cycles of the two optimal vectors. In Refs. [21,22], the weight coefficients in the cost function were optimized by either eliminating them or adjusting them based on the proposed principles, addressing the asymmetry in the dynamic characteristics of flux and torque. Reference [23] expanded the control set based on discrete space vector modulation (DSVM), the basic the number of voltage vectors was increased from 8 to 38, and to reduce the computational complexity, an optimization strategy for vectors' selection was employed. For DTP-PMSM, the number of basic voltage vectors could reach up to 64. If an exhaustive search is performed for all voltage vectors, it will result in a heavy computational burden. Therefore, it is necessary to optimize the computational load in multiphase motor control, such as reducing the number of candidate voltage vectors by using virtual voltage vectors or hyper-plane partitioning [24,25].

This paper focused on the DTP-PMSM with a 30° phase shift and proposed a dual-virtual-vector-based model predictive torque control (DVV-MPTC) strategy. First, virtual voltage vectors were introduced into the control set to address the issue of large harmonic current components. The cost function of the DVV-MPTC was also improved by shifting the control objective from magnitudes of torque and stator flux to the control of the stator flux vectors, thereby eliminating the weight coefficients. To address the issues of torque tracking error and insufficient current sinusoidal waveform, the dual vectors-based control concept was introduced to construct the DVV-MPTC strategy, which can reduce computational complexity and simultaneously suppress harmonic current components and torque ripples.

This paper was organized as follows: Section 2 introduced the mathematical models of this studied DTP-PMSM and corresponding output voltage vectors with a six-phase two-level inverter. Section 3 presented the single-virtual-vector-based model predictive torque control (SVV-MPTC). In Section 4, the DVV-MPTC was proposed along with the design of the cost function. Section 5 provided a comparative analysis of the results, which

demonstrates the superiority of the proposed control strategy. Finally, Section 6 presented some conclusions.

2. Mathematical Models and Inverter Output Voltage Vector

2.1. Mathematical Models of the Dual Three-Phase PMSM

The studied DTP-PMSM was driven by a six-phase two-level inverter, as shown in Figure 1, and it had two sets of three-phase stator windings, which have 30 electrical degrees apart, and the neutral points were isolated from each other.
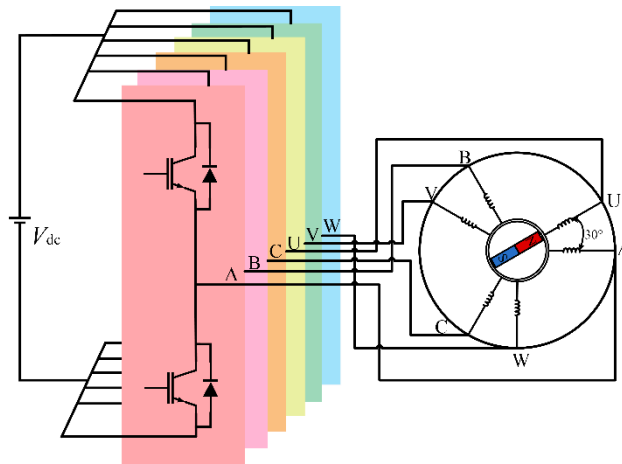
Figure 1. Six-phase two-level inverter-driven dual three-phase PMSM.

With the vector space decomposition (VSD) theory, mathematical models, including stator voltage, stator flux linkage, and electromagnetic torque, can be expresses as following.

$$\begin{bmatrix} u_d \\ u_q \end{bmatrix} = \begin{bmatrix} R_s & 0 \\ 0 & R_s \end{bmatrix} \cdot \begin{bmatrix} i_d \\ i_q \end{bmatrix} + \begin{bmatrix} L_d & 0 \\ 0 & L_q \end{bmatrix} \cdot \frac{d}{dt} \begin{bmatrix} i_d \\ i_q \end{bmatrix} + \begin{bmatrix} -\omega_e L_q i_q \\ \omega_e L_d i_d + \omega_e \psi_f \end{bmatrix} \tag{1}$$

$$\begin{bmatrix} u_x \\ u_y \end{bmatrix} = \begin{bmatrix} R_s & 0 \\ 0 & R_s \end{bmatrix} \cdot \begin{bmatrix} i_x \\ i_y \end{bmatrix} + \begin{bmatrix} L_z & 0 \\ 0 & L_z \end{bmatrix} \cdot \frac{d}{dt} \begin{bmatrix} i_x \\ i_y \end{bmatrix} \tag{2}$$

$$\begin{bmatrix} \psi_d \\ \psi_q \\ \psi_x \\ \psi_y \end{bmatrix} = \begin{bmatrix} L_d & 0 & 0 & 0 \\ 0 & L_q & 0 & 0 \\ 0 & 0 & L_z & 0 \\ 0 & 0 & 0 & L_z \end{bmatrix} \begin{bmatrix} i_d \\ i_q \\ i_x \\ i_y \end{bmatrix} + \begin{bmatrix} 1 \\ 0 \\ 0 \\ 0 \end{bmatrix} \psi_f \tag{3}$$

$$T_e = 3p_n i_q [i_d(L_d - L_q) + \psi_f] \tag{4}$$

where, u_d, u_q, u_x, u_y represent the voltage components in d-q and x-y coordinates, whereas i_d, i_q, i_x, and i_y are the corresponding current components. L_d and L_q are the inductances in d-q coordinate (here, $L_d = L_q$ for the surface-mounted structure), and L_z is the leakage inductance. R_s is stator resistance, ω_e is the angular velocity. ψ_f represents the magnitude of the permanent magnet flux linkage, and ψ_d, ψ_q, ψ_x, and ψ_y represent the flux components in d-q and x-y coordinates. T_e is the output electromagnetic torque, and p_n is the pole pairs of the motor.

### 2.2. Inverter Output Voltage Vectors

As shown in Figure 1, the six-phase two-level inverter has two states for each phase, represented by 1 and 0, respectively. Defining $(S_A S_B S_C S_U S_V S_W)$ as a set of switching sequences, the range of switching sequences is from (000000) to (111111), resulting in a

total of 2^6 = 64 switching states. Each switching state corresponds to a space voltage vector. From (5), the voltage vectors in the α-β subspace and x-y subspace can be obtained, with their distribution shown in Figure 2.

$$\begin{cases} v_{\alpha\beta} = \frac{1}{3}V_{dc}(S_A + S_B e^{j\frac{2\pi}{3}} + S_C e^{j\frac{4\pi}{3}} + S_U e^{j\frac{\pi}{6}} + S_V e^{j\frac{5\pi}{6}} + S_W e^{j\frac{3\pi}{2}}) \\ v_{xy} = \frac{1}{3}V_{dc}(S_A + S_B e^{j\frac{4\pi}{3}} + S_C e^{j\frac{2\pi}{3}} + S_U e^{j\frac{5\pi}{6}} + S_V e^{j\frac{\pi}{6}} + S_W e^{j\frac{3\pi}{2}}) \end{cases} \quad (5)$$
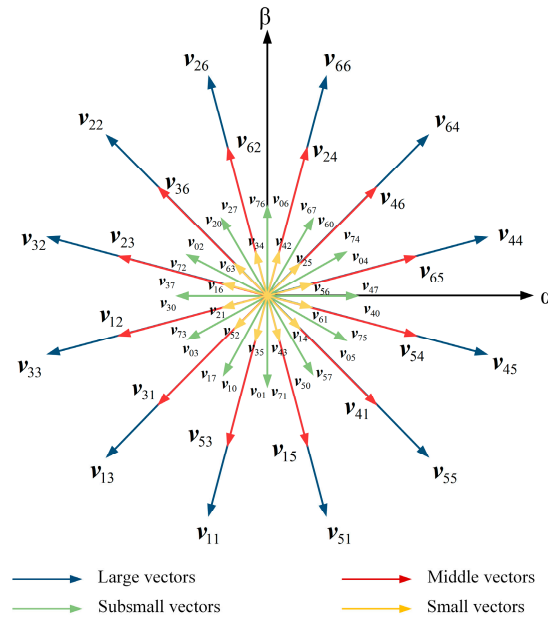
(a)
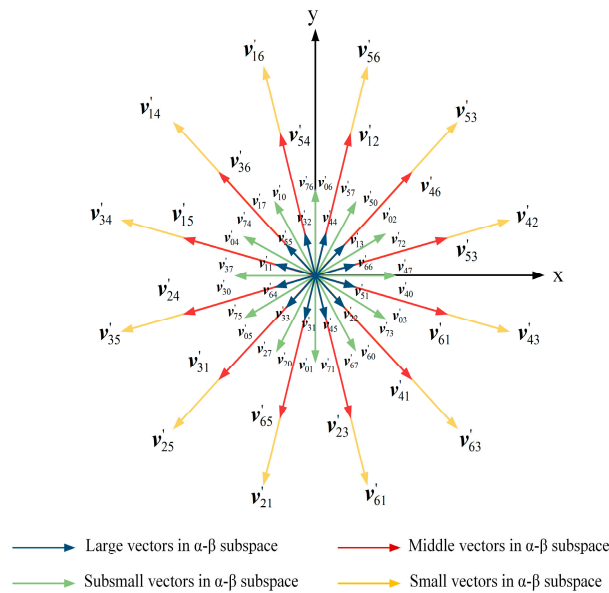
(b)

Figure 2. Voltage vectors' distribution: (**a**) α-β subplace and (**b**) x-y subplace.

From Figure 2, it can be observed that there are 60 non-zero voltage vectors and 4 zero vectors (v_{00}, v_{07}, v_{70}, v_{77}) in the α-β and x-y subspaces. The non-zero space voltage vectors can be divided into four groups based on their magnitudes: 12 large vectors, labeled v_{max}; 12 medium vectors, labeled v_{midl}; 24 sub-small vectors, labeled v_{mids}; and 12 small vectors, labeled v_{min}. The specific magnitudes of these four types of vectors are listed in Table 1.

Table 1. Four basic voltage vector magnitudes.

| Vector Types	Magnitudes
Large vectors $V_{\max}$	$\lvert V_{\max}\rvert = \frac{\sqrt{2}(\sqrt{3}+1)}{6}V_{dc} \approx 0.644V_{dc}$
Middle vectors V_{midl}	$\lvert V_{\mathrm{midl}}\rvert = \frac{\sqrt{2}}{3}V_{dc} \approx 0.471V_{dc}$
Subsmall vectors V_{mids}	$\lvert V_{\mathrm{mids}}\rvert = \frac{1}{3}V_{dc} \approx 0.333V_{dc}$
Small vectors $V_{\min}$	$\lvert V_{\min}\rvert = \frac{\sqrt{2}(\sqrt{3}-1)}{6}V_{dc} \approx 0.173V_{dc}$

3. Single-Virtual-Vector-Based MPTC

3.1. Virtual Vector's Synthesizing

It can be seen from formula (2) that the factors affecting the harmonic current components include the harmonic voltages u_{x}, u_{y}, stator resistance R_{s}, leakage inductance L_{z}, etc. To suppress the harmonic current components as much as possible, virtual voltage vectors that satisfy the harmonic voltage magnitude $\lvert v_{\mathrm{xy}}\rvert = 0$ were firstly synthesized.

As shown in Figure 2, the direction and magnitude of the voltage vector mapped in different subspaces for the same switching state might be different. The principle of the virtual vectors' synthesizing can be summarized as follows:

(1)   The synthesized virtual vectors' amplitudes should be as large as possible to ensure voltage utilization efficiency;

(2)   The synthesized virtual vectors' amplitudes in x-y subspace should be small to suppress harmonic current components.

Taking the large vector v_{44} and the medium vector v_{65} in α-β subspace as examples, the specific synthesizing process is shown in Figure 3.
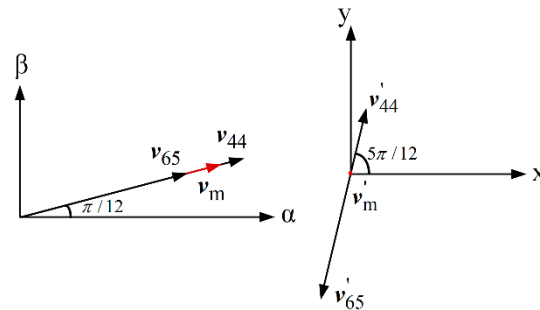
Figure 3. Synthesizing process of virtual vectors.

Assuming that within a period T_{s}, v_{44} is active for a time of μT_{s}, and then v_{65} is active for a time of $(1 - \mu)\,T_{\mathrm{s}}$. According to the volt-second balancing principle, the synthesized virtual vector v_{ml} can be derived as follows:

$$\begin{cases} \lvert v_{\mathrm{m1}-\alpha\beta}\rvert = \mu\lvert v_{44-\alpha\beta}\rvert + (1-\mu)\lvert v_{65-\alpha\beta}\rvert = \\ \qquad \frac{2}{3}V_{\mathrm{dc}}\left[\mu\cos\frac{\pi}{12} + (1-\mu)\cos\frac{\pi}{4}\right] \\ \lvert v_{\mathrm{m1}-\mathrm{xy}}\rvert = \mu\lvert v_{44-\mathrm{xy}}\rvert + (1-\mu)\lvert v_{65-\mathrm{xy}}\rvert = \\ \qquad \frac{2}{3}V_{\mathrm{dc}}\left[\mu\cos\frac{5\pi}{12} + (1-\mu)\cos\frac{\pi}{4}\right] \end{cases} \tag{6}$$

Let $\lvert v_{\mathrm{m1}-\mathrm{xy}}\rvert = 0$, which yields $\mu = \sqrt{3} - 1$, and then $\lvert v_{\mathrm{m1}-\alpha\beta}\rvert = \left(\sqrt{2} - \sqrt{6}/3\right)V_{\mathrm{dc}}$. By using this method, 12 virtual voltage vectors can be obtained, and their distribution is shown in Figure 4.
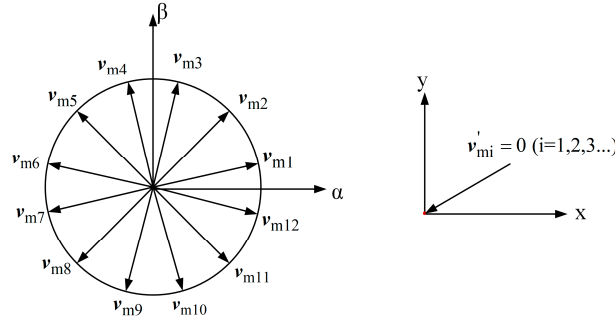
Figure 4. Virtual-voltage-vector spatial distribution.

3.2. Single-Virtual-Vector-Based MPTC Strategy

By discretizing the motor stator voltage equations using the forward Euler formula, the current prediction model in the d-q axis can be obtained:

$$
\begin{cases}
i_d^{k+1} = i_d^k + \frac{T_s}{L_s}\left[u_d^k - R_s i_d^k + \omega_e L_s i_q^k\right] \\
i_q^{k+1} = i_q^k + \frac{T_s}{L_s}\left[u_q^k - R_s i_q^k - \omega_e L_s i_d^k - \omega_e \psi_f\right]
\end{cases}
\tag{7}
$$

where u_d^k, u_q^k represent the voltage components in the d-q axis at kth sampling time, whereas i_d^k, i_q^k and i_d^{k+1}, i_q^{k+1} represent the corresponding current components at kth and $(k + 1)$th sampling time, respectively, and T_s is the sampling period.

Ideally, in MPC, actions such as signal acquisition, algorithm computation, and control state output can be completed instantaneously at the beginning of each sampling period. However, due to the presence of computational delay, the actual application of the optimal vector lags behind the sampling moment. Therefore, this paper adopted a two-step prediction method for delay compensation. After compensation, the current prediction model is expressed as follows:

$$
\begin{cases}
i_d^{k+2} = i_d^{k+1} + \frac{T_s}{L_s}\left[u_d^{k+1} - R_s i_d^{k+1} + \omega_e L_s i_q^{k+1}\right] \\
i_q^{k+2} = i_q^{k+1} + \frac{T_s}{L_s}\left[u_q^{k+1} - R_s i_q^{k+1} - \omega_e L_s i_d^{k+1} - \omega_e \psi_f\right]
\end{cases}
\tag{8}
$$

And T_e^{k+2}, $|\boldsymbol{\psi}_s^{k+2}|$ can be obtained based on the mathematical models in Section II.

$$
T_e^{k+2} = 3p_n i_q^{k+2} \psi_f
\tag{9}
$$

$$
\begin{cases}
\psi_d^{k+2} = L_d i_d^{k+2} + \psi_f \\
\psi_q^{k+2} = L_q i_q^{k+2}
\end{cases}
\tag{10}
$$

$$
\left|\boldsymbol{\psi}_s^{k+2}\right| = \sqrt{\left(\psi_d^{k+2}\right)^2 + \left(\psi_q^{k+2}\right)^2}
\tag{11}
$$

With the consideration that those synthesized virtual voltage vectors can significantly suppress the harmonic current components, the cost function of normal single-virtual-vector-based MPTC (SVV-MPTC) can be designed as follows:

$$
J_1 = \left|T_e^* - T_e^{k+2}\right| + \lambda_1 \left|\left|\boldsymbol{\psi}_s^*\right| - \boldsymbol{\psi}_s^{k+2}\right|
\tag{12}
$$

where λ_1 is the weight coefficient, whereas T_e^*, $|\boldsymbol{\psi}_s^*|$ are corresponding target values.

This MPTC strategy is based on single virtual voltage vector, which can effectively suppress harmonic current components. However, the problem of large torque ripples

still remains, which would significantly influence the control performance. Meanwhile, the weight coefficient needs to be designed to achieve satisfactory control performance. Therefore, tuning the weight coefficient is also a significant challenge for this method.

4. Double-Virtual-Vector-Based MPTC

To address above control issues, an improved double-virtual-vector-based MPTC strategy is proposed, including two aspects for improvement: (1) cost function is redesigned to avoid the weight coefficient by utilizing the mathematical models; (2) a double-virtual-vector-based MPTC strategy is employed to further reduce torque fluctuation.

4.1. Redesigning of Cost Function

According to the mathematical models, it can be seen that torque T_e is related to both the stator flux amplitude $|\psi_s|$ and the load angle δ. Therefore, torque T_e can also be expressed as follows:

$$T_e = \frac{3p_n}{L_q}|\boldsymbol{\psi}_s|\psi_f \sin\delta \tag{13}$$

The differential equation of torque can be obtained by taking the derivative of δ in (13) as follows:

$$\frac{dT_e}{d\delta} = \frac{3p_n|\boldsymbol{\psi}_s|\psi_f}{L_q} \cos\delta \tag{14}$$

Rewriting (14) into a difference form yields the following:

$$\Delta\delta = \frac{3\Delta T_e L_q}{p_n|\boldsymbol{\psi}_s|\psi_f \cos\delta} \tag{15}$$

where $\Delta\delta$ represents the load angle increment, and ΔT_e represents the torque increment.

Thus, the reference value of the load angle δ is expressed as follows:

$$\delta_{\text{ref}} = \delta + \Delta\delta \tag{16}$$

According to (16), the reference stator flux linkage components in the d-q axis can be expressed as follows:

$$\begin{cases} \psi_d^* = |\boldsymbol{\psi}_s^*| \cos\delta_{\text{ref}} \\ \psi_q^* = |\boldsymbol{\psi}_s^*| \cos\delta_{\text{ref}} \end{cases} \tag{17}$$

Based on the above analysis, the cost function without weighting coefficients can be constructed as follows:

$$J = \left|\psi_d^* - \psi_d^{k+2}\right| + \left|\psi_q^* - \psi_q^{k+2}\right| \tag{18}$$

4.2. Double-Virtual-Vector-Based MPTC Strategy

To improve the control performance, a double-virtual-vector-based MPTC (DVV-MPTC) strategy was proposed in this paper, where two virtual voltage vectors were applied within the same control period.

The first optimal voltage vector's selection of DVV-MPTC is the same as SVV-MPTC, which means that the voltage vector that minimizes the cost function would be chosen as the optimal voltage vector. The second optimal voltage vector in DVV-MPTC will be selected from the remaining 11 virtual voltage vectors, which has a selection method that can be summarized as follows.

By differentiating (4) and substituting it into (1), it can be obtained as follows:

$$\frac{dT_e}{dt} = \frac{3p_n\psi_f}{L_q}\left(u_q^{k+1} - R_s i_q^{k+1} - \omega_e \psi_d^{k+1}\right) \tag{19}$$

Thus, the slopes of T_e corresponding to two optimal voltage vectors can be expressed as follows:

$$\begin{cases} s_{T1} = \frac{3p_n\psi_f}{L_q}\left(u_{q1}^{k+1} - R_s i_q^{k+1} - \omega_e \psi_d^{k+1}\right) \\ s_{T2} = \frac{3p_n\psi_f}{L_q}\left(u_{qj}^{k+1} - R_s i_q^{k+1} - \omega_e \psi_d^{k+1}\right) \end{cases} \tag{20}$$

where u_{d1} and u_{q1} are the corresponding components in the d-q axis when the first optimal voltage vector is applied. Similarly, u_{dj} and u_{qj} are the corresponding components when the second optimal voltage vector is selected as the j-th voltage vector.

In this paper, the action times are calculated using deadbeat torque control. If the action times of the two optimal voltage vectors are assumed to be t_{opt1} and t_{opt2}, respectively, then

$$T_e^{k+2} = T_e^{k+1} + s_{T1}t_{opt1} + s_{T2}t_{opt2} = T_e^* \tag{21}$$

where T_e^{k+1} is the actual value of the torque at $(k + 1)^{th}$ sampling time.

By solving (21), there are 11 possible combinations of application times for the two optimal voltage vectors, which can be calculated as follows:

$$t_{opt1} = \frac{T_e^* - T_e^{k+1} - s_{T2}T_s}{(s_{T1} - s_{T2})T_s} \tag{22}$$

$$t_{opt2} = T_s - t_{opt1} \tag{23}$$

On the other hand, the slopes of ψ_d and ψ_q, when applying the two optimal voltage vectors, can be obtained as by combining (1) and (3).

$$\begin{cases} s_{d1} = u_{d1}^{k+1} - R_s i_d^{k+1} + \omega_e L_q i_q^{k+1} \\ s_{q1} = u_{q1}^{k+1} - R_s i_q^{k+1} - \omega_e L_d i_d^{k+1} - \omega_e \psi_f \end{cases} \tag{24}$$

$$\begin{cases} s_{dj} = u_{dj}^{k+1} - R_s i_d^{k+1} + \omega_e L_q i_q^{k+1} \\ s_{qj} = u_{qj}^{k+1} - R_s i_q^{k+1} - \omega_e L_d i_d^{k+1} - \omega_e \psi_f \end{cases} \tag{25}$$

where s_{d1} and s_{q1} represent the slopes of ψ_d and ψ_q when the first optimal voltage vector is applied, and s_{dj} and s_{qj} represent the slopes of ψ_d and ψ_q when the second optimal voltage vector is selected as the j-th voltage vector.

Then, the predicted flux linkage components in the d-q axis can be calculated as follows:

$$\begin{cases} \psi_d^{k+2} = \psi_d^{k+1} + s_{d1}t_{opt1} + s_{dj}t_{opt2} \\ \psi_q^{k+2} = \psi_q^{k+1} + s_{q1}t_{opt1} + s_{qj}t_{opt2} \end{cases} \tag{26}$$

By substituting (26) into the cost function, the second optimal voltage vector can be obtained. The selection process diagram for DVV-MPTC is shown in Figure 5.

The implementation process is summarized in Figure 6, and the control block diagram of DVV-MPTC method is shown in Figure 7.
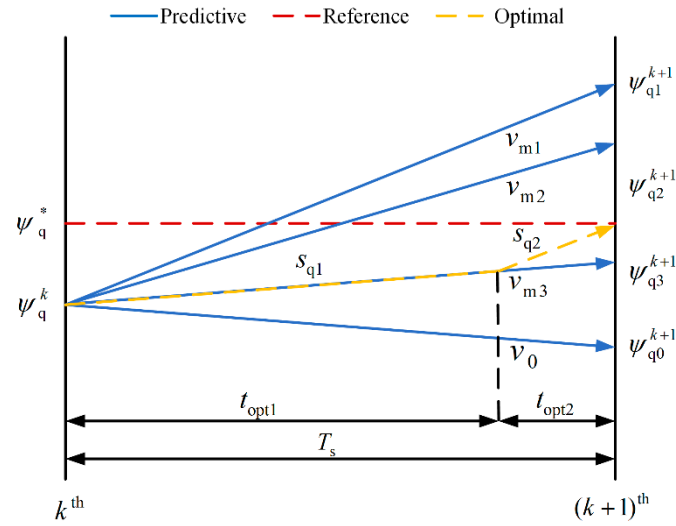
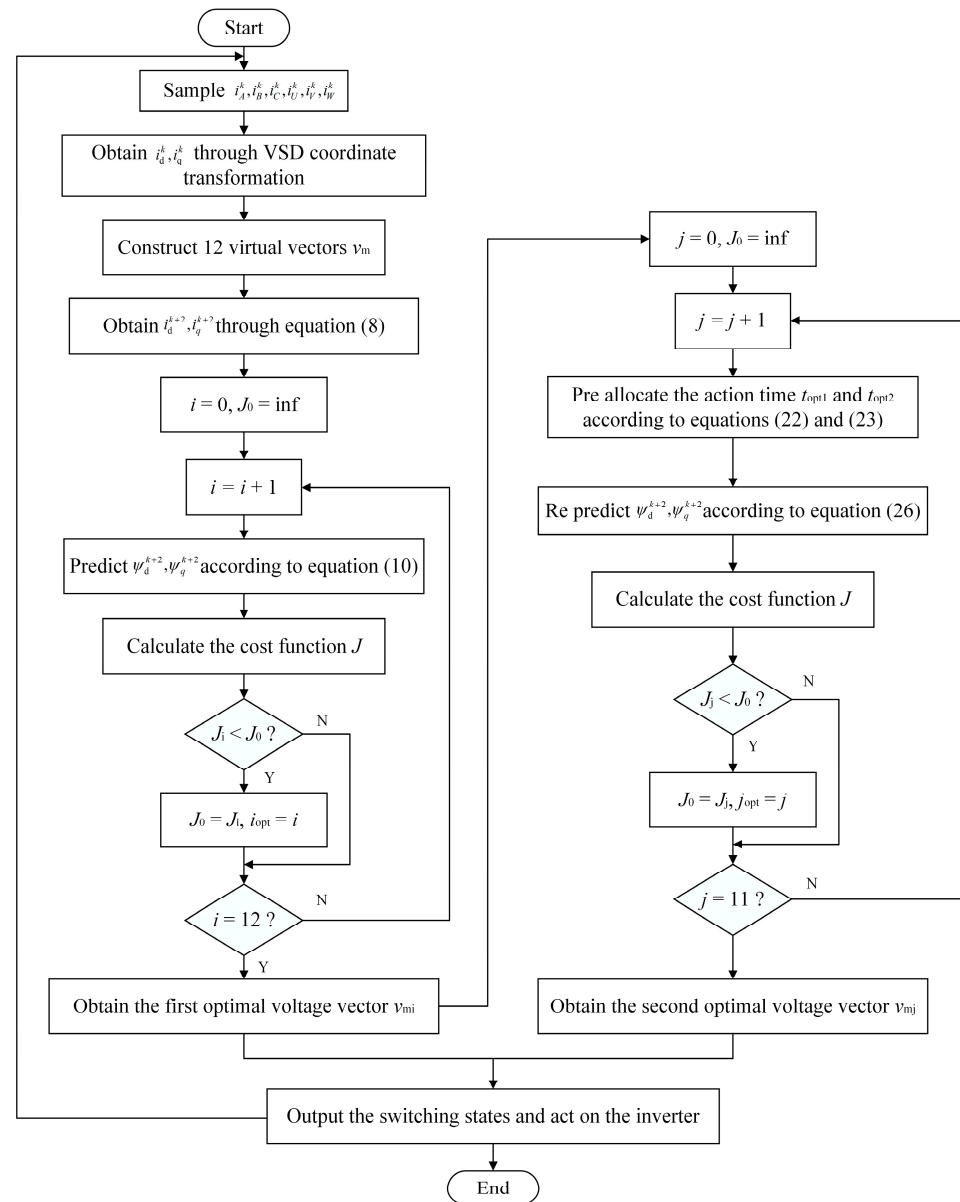**Figure 5.** Selection diagram of DVV-MPTC strategy.
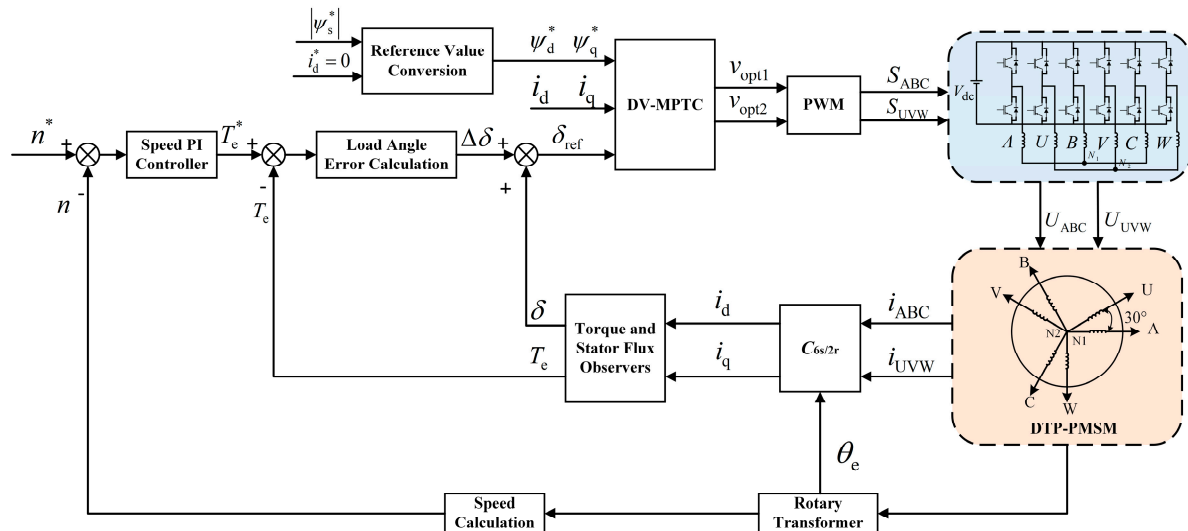

Figure 6. DVV-MPTC flowchart.

Figure 7. DVV-MPTC control block diagram.

5. Analysis of Results

To validate the efficacy and practicality of the proposed strategy, an experimental platform was set up, as illustrated in Figure 8. Figure 9 presents the schematic diagram of the motor windings, and the motor detailed parameters are provided in Table 2. The main control chip utilized is the Xilinx Kintex 7 series FPGA. Comparative experiments were carried out between traditional DTC, SVV-MPTC, and DVV-MPTC.
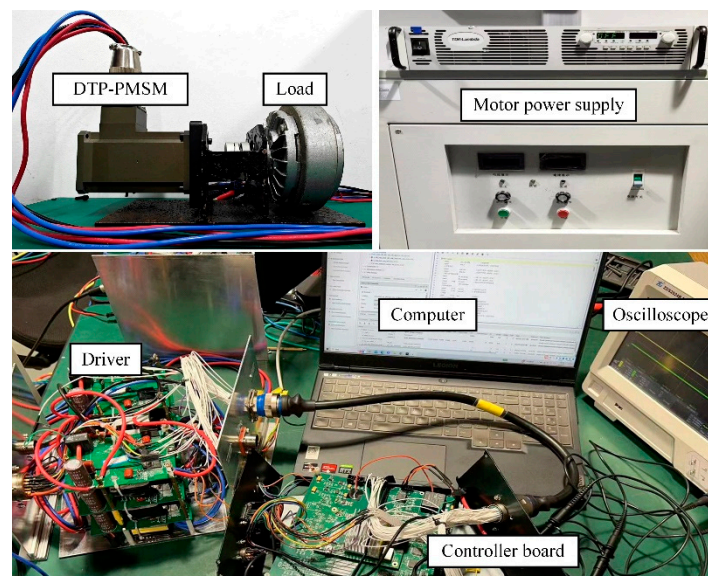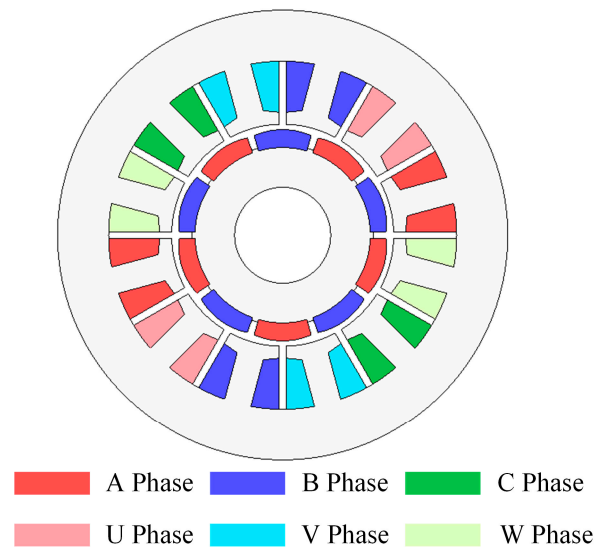

Figure 8. Experimental platform.

Firstly, the motor starts up to 11,000 r/min without a load, and at $t = 0.05$ s, a step load torque of 2 N·m is suddenly applied. The waveforms of the phase currents (i_A and i_U), electromagnetic torque, harmonic current components (i_x and i_y), and common-mode voltage u_{cmv} are compared in Figures 10–12, respectively.

Figure 9. Motor winding diagram.

Table 2. Detail parameters.

Parameters	Value
Pole pairs n_p	5
Stator resistance R_s	0.08 Ω
d-axis inductance L_d	0.33 mH
q-axis inductance L_q	0.33 mH
PMSM magnetic flux ψ_f	0.01215 Wb
DC-link voltage	270 V
Rotary inertia J_m	72.96 kg·mm^2
Rated speed n	12,000 r/min
Rated stator current I_N	12 A
Rated torque T_N	2.2 N·m
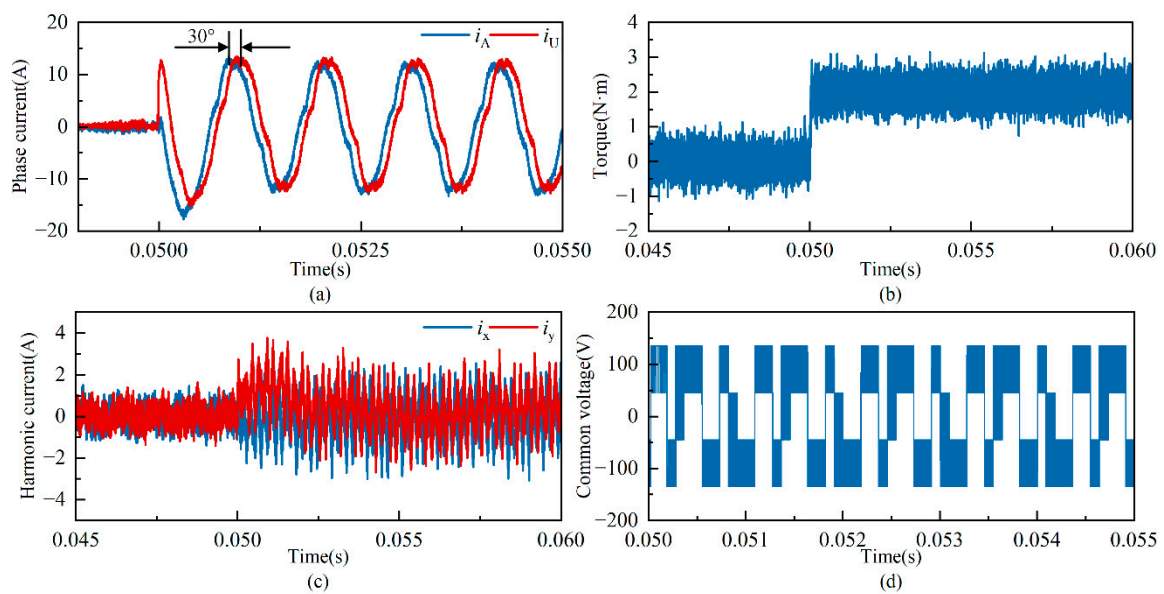
Figure 10. DTC method: (**a**) phase current; (**b**) electromagnetic torque; (**c**) harmonic current; (**d**) common-mode voltage.
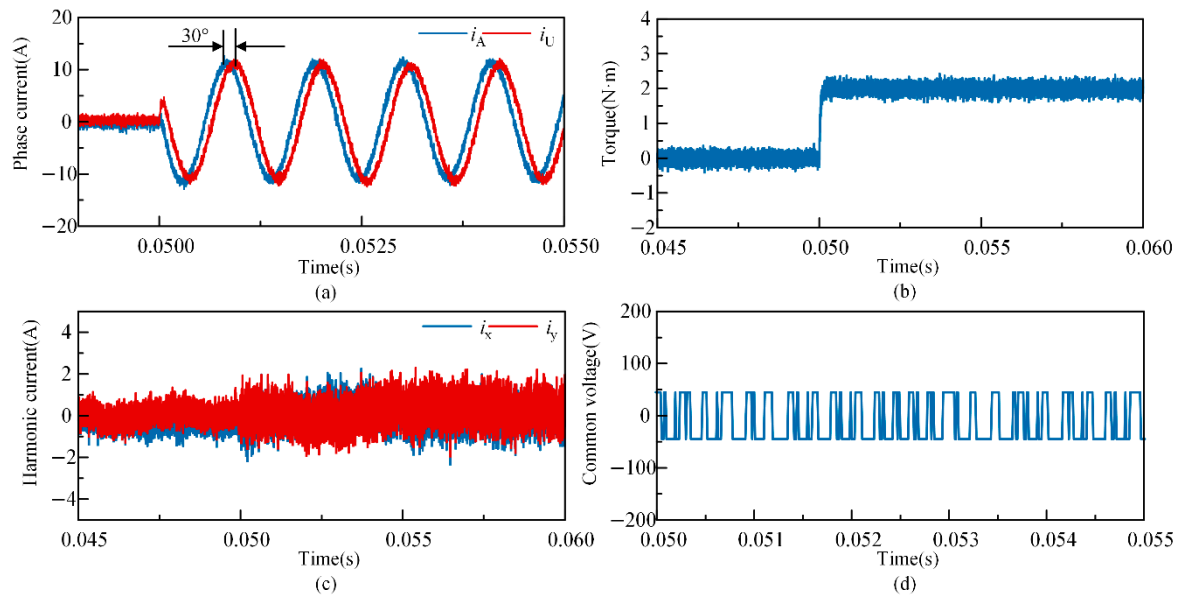
Figure 11. SVV-MPTC method: (**a**) phase current; (**b**) electromagnetic torque; (**c**) harmonic current; (**d**) common-mode voltage.
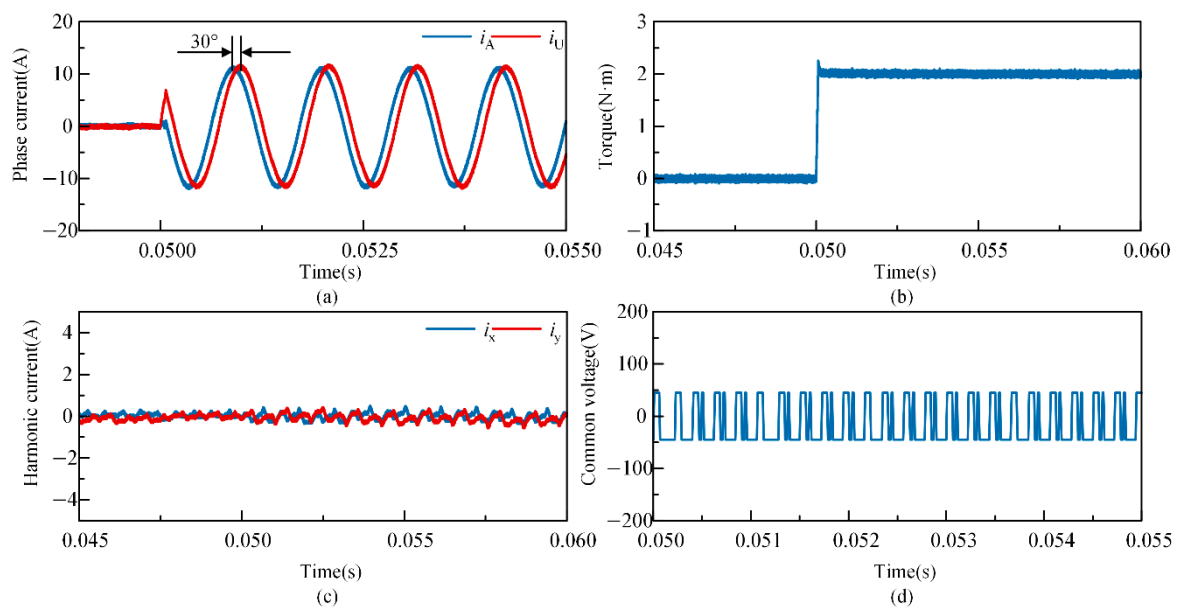
Figure 12. DVV-MPTC method: (**a**) phase current; (**b**) electromagnetic torque; (**c**) harmonic current; (**d**) common-mode voltage.

By comparing the results of these three control strategies, it can be observed that when a sudden 2 N·m load is applied at 0.05 s during no-load operation, the electromagnetic torque with all strategies quickly tracks the given load torque, whereas the proposed DVV-MPTC strategy effectively reduces torque ripples and shows better performance in terms of current quality.

The formula for calculating the total harmonic distortion (THD) of the phase current is shown below. Figure 13 presents the FFT analysis results of the phase A current under the three control strategies, with the calculated THD values indicated at the top of each

figure. The results are summarized in Table 3, which also provides the specific content of the fifth and seventh harmonics.

$$\text{THD} = \frac{\sqrt{I_2^2 + I_3^2 + I_4^2 + \cdots + I_n^2}}{I_1} \times 100\% \tag{27}$$

where I_1 is the root mean square (RMS) value of the fundamental current, and I_2, I_3, I_4, ..., I_n are the RMS values of the harmonic currents (corresponding to the second, third, fourth, up to the nth harmonics).
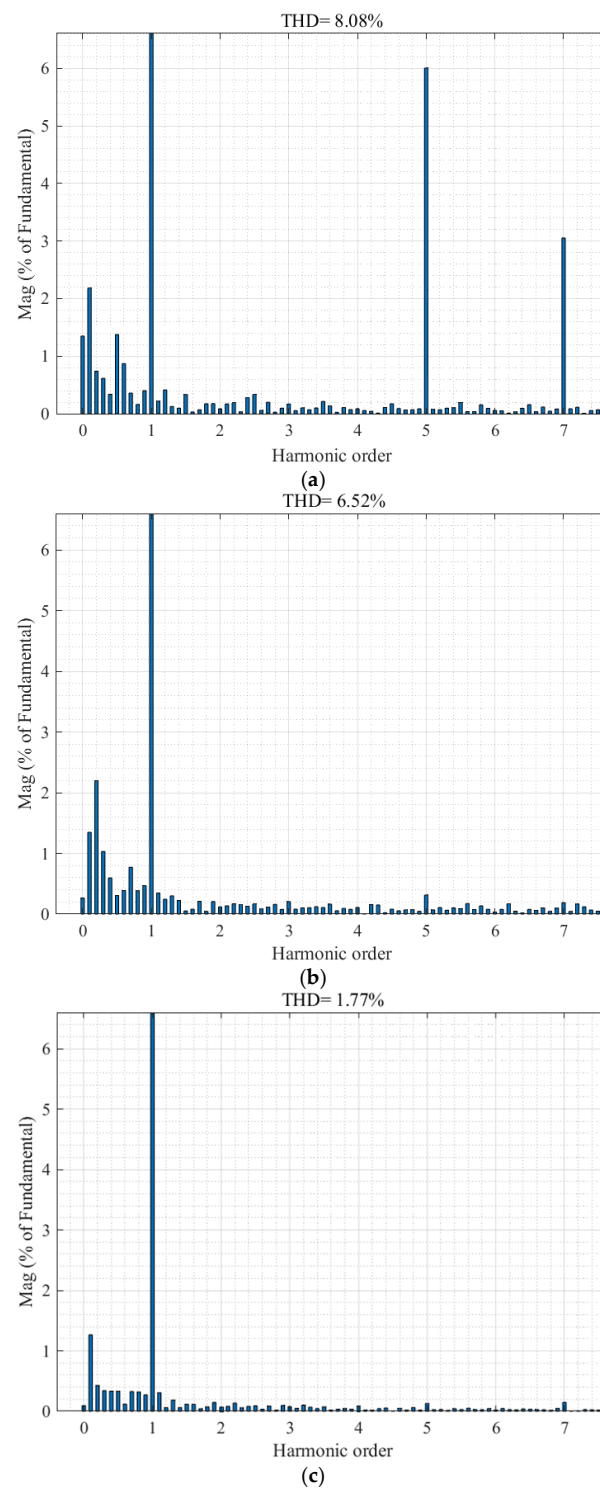
Figure 13. FFT analysis results: (**a**) DTC; (**b**) SVV-MPTC; (**c**) DVV-MPTC.

Table 3. THD values of different control strategies.

Strategy	THD of i_A	5th	7th
DTC	8.08%	6.00%	3.05%
SVV-MPTC	6.52%	0.32%	0.18%
DVV-MPTC	1.77%	0.13%	0.15%

Clearly, the THD values of SVV-MPTC and DVV-MPTC are smaller than traditional DTC. This is because the introduction of virtual voltage vectors ensures that the amplitude of the harmonic voltage in the x-y subspace is zero, effectively suppressing the fifth and seventh harmonics in the phase current. Furthermore, the introduction of dual-voltage vectors allows for more precise approximation of the target reference values. Compared to single voltage vector control, dual voltage vectors control provides more flexible voltage vector actions, better accommodating complex transient variations during motor operation. As a result, DVV-MPTC exhibits a lower higher-order harmonic content, particularly in the fifth and seventh harmonics.

Torque ripple is defined as follows:

$$T_{\text{ripple}} = (T_{\max} - T_{\min})/T_{\text{avg}} \times 100\% \tag{28}$$

where $T_{\max}$, $T_{\min}$, and T_{avg} are the maximum, minimum, and average values of the electromagnetic torque, respectively.

After calculation, among the three control strategies, the torque ripple value of DTC is the highest at 142.90%, whereas the value of SVV-MPTC strategies is 47.9%. For this proposed DVV-MPTC strategy, the torque ripple can be significantly reduced to 10.7%.

The DTP-PMSM studied in this paper featured double stator windings with isolated star points, resulting in the generation of significant common-mode voltage (CMV) in the inverter circuit, which could cause electromagnetic interference and leakage currents and other issues in the control system. With the utilization of virtual voltage vectors, this proposed DVV-MPTC strategy can avoid the use of zero vectors, thereby significantly reducing the magnitude of the CMV. As shown in Figures 10–12, before using virtual voltage vectors, the CMV ranges from −135 V to +135 V, whereas after improvement, the CMV range can be reduced to −45 V to +45 V.

If all categories of vectors are traversed for optimization, the real-time performance of the algorithm will significantly degrade, and the performance requirements for the processor will greatly increase. The introduction of virtual voltage vectors reduces the number of candidate voltage vectors in the control of DTP-PMSM. As a result, both SVV-MPTC and DVV-MPTC significantly reduce the computational load and improve the overall speed of the algorithm compared to traditional SV-MPTC. Although the computation time of DVV-MPTC is slightly higher than that of SVV-MPTC, considering the dynamic and steady-state performance of the control strategy, the slight increase in computational load is within an acceptable range. Table 4 provides the number of candidate voltage vectors and the average execution time required to obtain an optimal voltage vector for the three control strategies.

To verify the feasibility of the proposed control strategy for the drive system under different motor speed conditions, the experiments were conducted at motor speeds of 10% and 50% of the rated speed, i.e., 1200 r/min and 6000 r/min, respectively. The following Figures 14 and 15 present the experimental results of the motor phase current and torque.

Table 4. The number of candidate voltage vectors and the average execution time.

	The Number of Candidate Voltage Vectors	The Average Execution Time (μs)
SV-MPTC	64	6.206
SVV-MPTC	12	1.536
DVV-MPTC	12 × 11	2.184
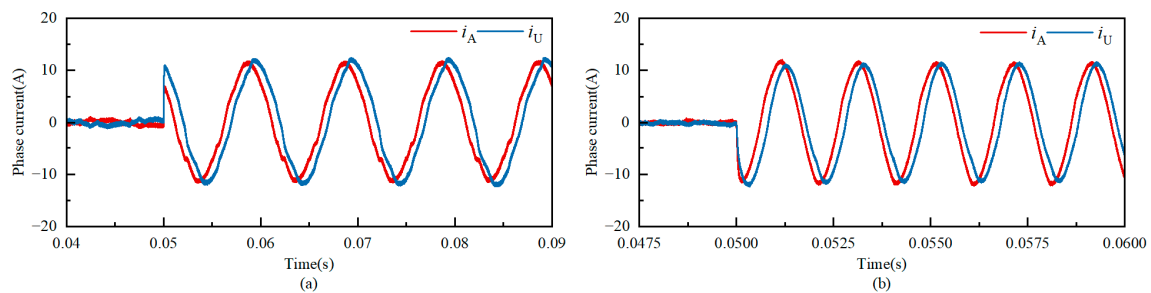
Figure 14. Motor phase current waveforms: (**a**) speed at 1200 r/min; (**b**) speed at 6000 r/min.
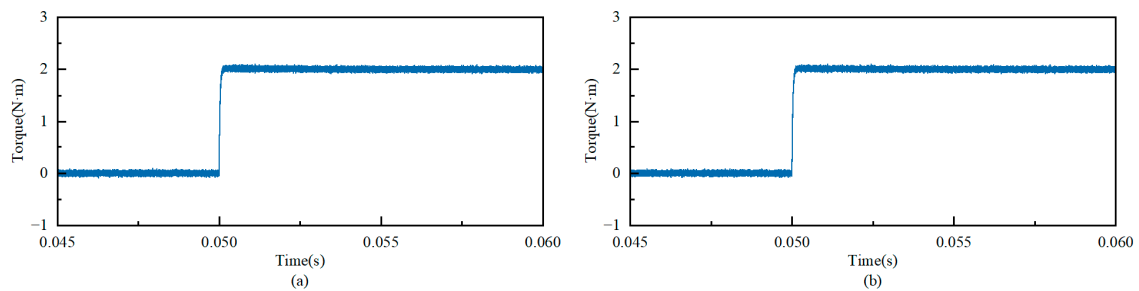
Figure 15. Motor output torque waveforms: (**a**) speed at 1200 r/min; (**b**) speed at 6000 r/min.

Analyzing the figures, it can be observed that the motor phase currents exhibit high sinusoidal quality, the torque shows good tracking performance, and the steady-state error is minimal, demonstrating that DVV-MPTC has good feasibility under different operating conditions.

Table 5 presents the FPGA resource utilization of the proposed control strategy drive system. The percentage usage indicates the efficiency of the proposed design in utilizing the available resources.

Table 5. Resource usage of the FPGA matrix.

Resource	Utilization	Available	Utilization (%)
LUT	74,106	203,800	36.36
LUTRAM	178	64,000	0.28
FF	77,271	407,600	18.96
BRAM	73	445	16.40
IO	69	500	13.80
BUFG	4	32	12.50
MMCM	1	10	10.00

From the data, it can be observed that the designed control system has relatively low resource utilization on the FPGA, with LUT and FF utilization rates of 36.36% and 18.96%, respectively. This indicates that the hardware implementation achieves good resource efficiency and provides sufficient resource margins for future functionality expansion.

6. Conclusions

This paper addressed the issue of high harmonic components in the stator current and large torque ripples in DTP-PMSM with traditional DTC method or SVV-MPTC method. With this proposed DVV-MPTC strategy, both the harmonic components in the stator and the output torque ripples were suppressed and improved. In particular, the total harmonic distortion was reduced to 1.77% for DVV-MPTC method, while it was 6.52% and 8.08% for SVV-MPTC method and traditional DTC method, respectively. The torque ripple can be significantly reduced to 10.7% with this proposed novel method, while it also maintains a fast dynamic response under sudden changes in load torque. Moreover, the drive system is applicable to different motor speed conditions.

Author Contributions: Conceptualization, Q.Y.; Methodology, R.X.; Software, R.X.; Validation, J.W.; Writing—original draft, R.X.; Writing—review & editing, Q.Y., J.W. and W.Y.; Project administration, K.X. All authors have read and agreed to the published version of the manuscript.

Data Availability Statement: The data presented in this study are available upon request from the corresponding author. The data are not publicly available due to the confidentiality restrictions of this study.

Conflicts of Interest: Author Wei Yu was employed by the company Hella Shanghai Electronics Co., Ltd. The remaining authors declare that the research was conducted in the absence of any commercial or financial relationships that could be construed as a potential conflict of interest.

References

1. Methsamphop, M.; Ufot, E.U.; Inamori, M. Characteristics of Two-Phase Inverter-Fed Three-Phase Induction Motor Drive. *J. Electr. Eng. Technol.* **2023**, *18*, 377–382. [CrossRef]
2. Wang, Z.W.; Jin, H.; Guo, J.; Su, J.; Wang, M. Research on Control System of Three-phase Brushless DC Motor for Electric Vehicle. *IOP Conf. Ser. Mater. Sci. Eng.* **2017**, *274*, 012016. [CrossRef]
3. Barrero, F.; Duran, M.J. Recent Advances in the Design, Modeling, and Control of Multiphase Machines—Part I. *IEEE Trans. Ind. Electron.* **2016**, *63*, 449–458. [CrossRef]
4. Shchur, I.; Jancarczyk, D. Electromagnetic Torque Ripple in Multiple Three-Phase Brushless DC Motors for Electric Vehicles. *Electronics* **2021**, *10*, 3097. [CrossRef]
5. Yang, R.; Schofield, N.; Zhao, N.; Emadi, A. Dual three-phase permanent magnet synchronous machine investigation for battery electric vehicle power-trains. *J. Eng.* **2019**, *2019*, 3981–3985. [CrossRef]
6. Levi, E.; Bojoi, R.; Profumo, F.; Toliyat, H.; Williamson, S. Multiphase induction motor drives—A technology status review. *IET Electr. Power Appl.* **2007**, *1*, 489–516. [CrossRef]
7. Singh, G.K. Multi-phase induction machine drive research—A survey. *Electr. Power Syst. Res.* **2002**, *61*, 139–147. [CrossRef]
8. Yu, K.; Wang, Z.; Gu, M.; Wang, X. Universal control scheme of dual three-phase PMSM drives with single open-phase fault. *IEEE Trans. Power Electron.* **2022**, *37*, 14034–14039. [CrossRef]
9. Loncarski, J.; Leijon, M.; Srndovic, M.; Rossi, C.; Grandi, G. Comparison of Output Current Ripple in Single and Dual Three-Phase Inverters for Electric Vehicle Motor Drives. *Energies* **2015**, *8*, 3832–3848. [CrossRef]
10. Keller, D.; Kuenzler, M.; Karayel, A.; Werner, Q.; Parspour, N. Potential of dual three-phase PMSM in high performance automotive powertrains. In Proceedings of the 2020 International Conference on Electrical Machines (ICEM), Gothenburg, Sweden, 23–26 August 2020; Volume 1, pp. 1800–1806.
11. Hwang, K.Y.; Song, B.K.; Kwon, B.I. Asymmetric dual winding three-phase PMSM for fault tolerance of overheat in electric braking system of autonomous vehicle. *IET Electr. Power Appl.* **2019**, *13*, 1891–1898. [CrossRef]
12. Shao, B.; Zhu, Z.Q.; Feng, J.; Guo, S.; Li, Y.; Liao, W. Compensation of Selective Current Harmonics for Switching-Table-Based Direct Torque Control of Dual Three-Phase PMSM Drives. *IEEE Trans. Ind. Appl.* **2021**, *57*, 2505–2515. [CrossRef]
13. Bian, C.; Zhao, G.; Li, X.; Man, Y. Research and design of DTC system based on six-phase asymmetrical BLDCM. *CES Trans. Electr. Machines Syst.* **2018**, *2*, 123–128. [CrossRef]
14. Wang, Y.; Huang, S.; Huang, X.; Liao, W.; Zhang, J.; Ma, B. An Angle-Based Virtual Vector Model Predictive Current Control for IPMSM Considering Overmodulation. *IEEE Trans. Transp. Electr.* **2024**, *10*, 353–363. [CrossRef]

15. Jia, B.L.; Xie, W. An improved seven-phase SVPWM modulation strategy based on virtual voltage vectors. *Energy Rep.* **2023**, *9*, 543–549. [CrossRef]

16. Yuan, Q.; Zhao, R.; Xiao, R.; Liu, Z. Zero Common-Mode Voltage Model Predictive Torque Control Based on Virtual Voltage Vectors for the Dual Three-Phase PMSM Drive. *Electronics* **2022**, *11*, 3293. [CrossRef]

17. Shao, B.; Zhu, Z.Q.; Yan, L.C.; Feng, J.H.; Guo, S.Y.; Li, Y.F. Torque Ripple Reduction for Direct Torque Control of Dual Three-Phase PMSM Based on Multiple Virtual Voltage Vectors. *IEEE Trans. Energy Convers.* **2023**, *38*, 296–309. [CrossRef]

18. Li, Y.H.; Liu, Z.K.; Wang, X.Y.; Chen, G.X.; Ren, C.; Liu, D.M. Simplified Control Strategy for Model Predictive Torque Control of Permanent Magnet Synchronous Motor. *Control. Theory Appl.* **2023**, *40*, 1793–1805.

19. Song, W.X.; Ren, H.; Yang, Y.; Lv, H.Z. Dual-Vector Model Predictive Torque Control of Dual Three-Phase Permanent Magnet Synchronous Motor Two vectors based model predictive torque control of dual three phase permanent magnet synchronous motor. *Electr. Mach. Control* **2022**, *26*, 97–107.

20. Farah, N.; Lei, G.; Zhu, J.; Guo, Y. Two-vector Dimensionless Model Predictive Control of PMSM Drives Based on Fuzzy Decision Making. *CES Trans. Electr. Machines Syst.* **2022**, *6*, 393–403. [CrossRef]

21. Li, X.L.; Xue, Z.W.; Yan, X.Y.; Feng, X.T.; Zhang, L.X. Three-Vector Model Predictive Torque Control of Permanent Magnet Synchronous Motor Based on Fast Voltage Vector Selection Voltage Vector Rapid Screening-Based Three-Vector Model Predictive Torque Control for Permanent Magnet Synchronous Motor. *Trans. China Electrotech. Soc.* **2022**, *37*, 1666–1678.

22. Gong, C.; Hu, Y.H.; Ma, M.Y.; Gao, J.Q.; Shen, K. Novel Analytical Weighting Factor Tuning Strategy based on State Normalization and Variable Sensitivity Balance for PMSM FCS-MPTC. *IEEE/ASME Trans. Mechatron.* **2020**, *25*, 1690–1694. [CrossRef]

23. Gu, M.; Yang, Y.; Fan, M.; Xiao, Y.; Liu, P.; Zhang, X.; Yang, H.; Rodriguez, J. Finite Control Set Model Predictive Torque Control With Reduced Computation Burden for PMSM Based on Discrete Space Vector Modulation. *IEEE Trans. Energy Convers.* **2023**, *38*, 703–712. [CrossRef]

24. Arahal, M.R.; Satué, M.G.; Barrero, F. Multi-phase weighted stator current tracking using a hyper-plane partition of the control set. *Control Eng. Pract.* **2024**, *153*, 106114. [CrossRef]

25. Arahal, M.R.; Barrero, F.; Satué, M.G.; Bermúdez, M. Fast Finite-State Predictive Current Control of Electric Drives. *IEEE Access* **2023**, *11*, 12821–12828. [CrossRef]